

Optimization of the Bulk Heterojunction Composition for Enhanced Photovoltaic Properties: Correlation between the Molecular Weight of the Semiconducting Polymer and Device Performance

Célia Nicolet,^{†,‡} Dargie Deribew,^{†,‡} Cedric Renaud,^{†,‡} Guillaume Fleury,^{*,†,‡} Cyril Brochon,^{†,‡} Eric Cloutet,^{†,‡} Laurence Vignau,^{§,||} Guillaume Wantz,^{§,||} Henri Cramail,^{†,‡} Mark Geoghegan,^{†,‡,⊥} and Georges Hadzioannou^{*,†,‡}

[†]Université de Bordeaux, Laboratoire de Chimie des Polymères Organiques, IPB/ENSCBP, 16 avenue Pey-Berland, F-33607 Pessac Cedex, France

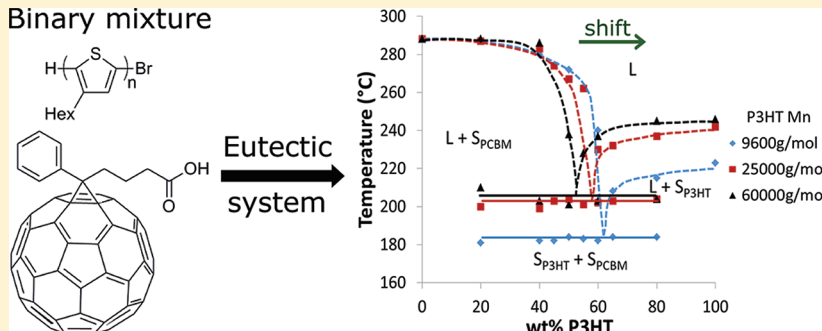
[‡]Centre National de la Recherche Scientifique, Laboratoire de Chimie des Polymères Organiques, UMR 5629, 16 avenue Pey-Berland, F-33607 Pessac Cedex, France

[§]Université de Bordeaux, Laboratoire de l'Intégration du Matériau au Système, IPB/ENSCBP, 16 avenue Pey-Berland, F-33607 Pessac Cedex, France

^{||}Centre National de la Recherche Scientifique, Laboratoire de l'Intégration du Matériau au Système, UMR 5218, 16 Avenue Pey Berland, Pessac Cedex, F-33607, France

 Supporting Information

ABSTRACT:



Herein we propose an approach toward the optimization of the photovoltaic performance of bulk heterojunctions by tuning the composition of the active layer with respect to the molecular weight of the semiconducting polymer. We used a poly(3-hexylthiophene):[6,6]-phenyl-C61-butyric acid methyl ester (P3HT:PCBM) blend as a typical system and varied the molecular weight of the P3HT semiconducting polymer in order to determine its influence on the bulk heterojunction morphology as well as on the optoelectronic characteristics of the device. We have systematically mapped out the phase diagram for different molecular weight P3HTs blended with PCBM and observed the presence of a eutectic composition, which shifts to higher content of P3HT for lower molecular weight P3HTs. This shift inherent to the P3HT molecular weight is also apparent in the photovoltaic performance as the eutectic composition corresponds to the best of the photovoltaic properties. The P3HT molecular weight dependence of the eutectic composition is due to the molecular weight dependence of the P3HT crystallization behavior, which leads to dramatic morphological changes of the bulk heterojunction.

INTRODUCTION

In 2005, a breakthrough in the efficiency of organic photovoltaic solar cells was achieved with a 5% power conversion efficiency (PCE) using a poly(3-hexylthiophene):[6,6]-phenyl-C61-butyric acid methyl ester (P3HT:PCBM) (1:0.8) blend used as the active layer.¹ Numerous parameters were optimized (blend composition, annealing time, and temperature) in order to obtain this state of the art performance. Consequently, the results suggest that the phase separation between P3HT and PCBM leading to the bulk heterojunction mesostructure is

strongly correlated with the device fabrication process.² To maximize the exciton diffusion/dissociation as well as charge transport to the respective electrodes, different studies have shown that the optimum phase separation between the donor and the acceptor domains should be bicontinuous with nanosized structures.^{3–7} Even if this structure is highly desired for

Received: August 10, 2011

Revised: September 21, 2011

Published: September 22, 2011

optimizing the photovoltaic processes, recent studies have shown that a hierarchical nanomorphology with miscible polymer/fullerene derivatives domains depict more accurately the actual morphology of these binary blends.^{8,9}

The annealing treatment is one of the key parameters required to achieve this nanosized bicontinuous morphology, partly because the choice of appropriate annealing time and temperature promotes the crystallization of the polymer^{1,3,10–12} and facilitates phase separation as well as diffusion between P3HT and PCBM at either nanoscopic^{3,13,14} or microscopic scales.¹⁵ Phase separation occurs with the diffusion of PCBM¹⁵ induced by the crystallization of P3HT¹⁶ leading to the formation of microsized PCBM agglomerates^{17–21} while the nanoscale separation is induced by the P3HT crystallization. Indeed, even if P3HT and PCBM are compatible from a thermodynamic point of view,^{22,23} the $\pi-\pi$ interactions between the P3HT chains promoted by the P3HT crystallization leads to a phase segregation between P3HT and PCBM. As a consequence, PCBM is ejected following either spinodal decomposition in the case of deep quenching or nucleation and growth (binodal decomposition) in the case of slow cooling.^{22,24,25} Other parameters such as the solvent,^{22,26} the composition of the active layer in P3HT and PCBM binary blends,^{14,27} or the P3HT molecular weight (M_n)^{28–33} also influence the resulting morphology.

So far, most experiments on P3HT:PCBM-based organic solar cells have been performed at a composition of 1:1 (50 wt % of P3HT)³⁴ or 1:0.8 (56 wt % of P3HT).¹ A few studies show that the best performance could be obtained with around 60 wt % of P3HT.^{14,35} Stutzmann et al. explored the binary phase diagram for a P3HT:PCBM blend and demonstrated its eutectic nature.³⁶ Characterization of P3HT:PCBM blends by grazing incidence X-ray scattering and X-ray diffraction have shown that high molecular weight P3HTs exhibit amorphous domains connecting the crystalline parts together leading to a bicontinuous network of P3HT and PCBM. Consequently, the exciton dissociation and bipolar charge transport are improved and PCE tends to increase with molecular weight.^{28–32}

Herein we describe a systematic study to understand how the P3HT molecular weight influences the photovoltaic performance. We correlate the macromolecular characteristics of the P3HT to the morphology of the active layer as well as with the photovoltaic characteristics. We have synthesized five P3HTs with different molecular weights in the range of 5.8 to 60 kg/mol, and we have studied their phase behavior in a binary system with PCBM. We have established the phase diagram between these P3HTs and PCBM and used scanning force microscopy (SFM) and transmission electron microscopy (TEM) to map out their respective morphology in the thin film configuration. Additionally, we have determined the photovoltaic performance of the same thin films as the ones used for SFM and TEM characterization. Consistency between the results of the different experiments was rigorously ensured by keeping an identical sample preparation process (see Experimental Section). A relevant and reproducible PCE of 3% has been reached for the optimal parameters. We show that the best composition in P3HT and PCBM is not absolute but depends on the P3HT molecular weight and dispersity.

EXPERIMENTAL SECTION

Materials. All reactions were carried out under a dry nitrogen atmosphere, using flame-dried glassware. Tetrahydrofuran

(THF), *tert*-butylmagnesium chloride (1 M in THF), 1,3-bis(diphenylphosphino)propane nickel(II) dichloride ($Ni(dppp)Cl_2$), and *ortho*-dichlorobenzene (*o*-DCB) were purchased from Aldrich (France), PCBM from Solaris, P3HT-10k was purchased from Plextronics (molecular weight $M_n = 105$ kg/mol, dispersity $D = 1.9$ and regioregularity =98%), indium tin oxide (ITO) (10 Ω/sq) coated on a glass substrate (15 mm \times 15 mm \times 0.7 mm) was purchased from Kintec Company, and poly(3,4-ethylenedioxythiophene):poly(styrene sulfonate) (PEDOT:PSS) was purchased from H.C. Starck GmbH. THF was distilled over its drying agents under reduced pressure. PEDOT:PSS was filtered over a syringe filter with a regenerated cellulose (RC) membrane (0.2 μm pore size). All the other reagents were used as supplied without further purification.

Synthesis of P3HT. 2,5-Dibromo-3-hexylthiophene was prepared as already reported.³⁷ P3HT-60k was synthesized according to the Grignard metathesis route.^{38–40} A 5.21 g (16 mmol) portion of the 2,5-dibromo-3-hexylthiophene was dissolved in 20 mL of THF and stirred under nitrogen. Sixteen milliliters (16 mmol) of *tert*-butylmagnesium chloride was added, and the reaction was stirred at room temperature for 2 h. The mixture was then diluted in 60 mL of THF, 25 mg of $Ni(dppp)Cl_2$ (0.045 mmol, 0.28% on monomer) was added, and the mixture was stirred for 1 h at room temperature. Addition of 2 mL of degassed methanol terminated the polymerization. The polymer was recovered by precipitation in methanol, washed with a Soxhlet procedure with pentane for 48 h, then dissolved with chloroform and recovered by precipitation in methanol. P3HT-5.8k, P3HT-9.6k, P3HT-25k, and P3HT-40k were synthesized in the same way as P3HT-60k, by adjusting the weight ratios of the $Ni(dppp)Cl_2$ /monomer accordingly, i.e., 3.1%, 1.8%, 1.1%, and 0.52%, respectively.

Characterization of P3HT. ^1H nuclear magnetic resonance (^1H NMR) spectra were recorded using a Bruker AC-400 NMR at room temperature, and the samples were dissolved in deuterated chloroform $CDCl_3$. Size exclusion chromatography (SEC) was performed in THF at 40 °C at a flow rate of 1 $\text{mL} \cdot \text{min}^{-1}$ using a differential refractometer (Varian) and a UV-visible spectrophotometer (Varian) operating at 254 nm and using 3 TSK gel Tosoh columns (G4000HXL, G3000HXL, and G2000HXL). The elution times were converted into molecular weights using a calibration curve based on low dispersity polystyrene standards.

The molecular weight and the dispersity were analyzed by SEC. The regioregularity was calculated by integration of the corresponding peaks on the ^1H NMR spectrum. The molecular weights of P3HT-5.8k, P3HT-9.6k, P3HT-25k, P3HT-40k, and P3HT-60k are respectively 5.8 kg/mol, 9.6 kg/mol, 25 kg/mol, 40 kg/mol and 60 kg/mol, their dispersities were measured to be 1.6, 1.3, 1.1, 1.4, and 1.4, respectively, and their regioregularities were 89%, 92%, 96%, 98% and 99%.

Differential Scanning Calorimetry (DSC) Measurements. Samples for the DSC analyses were prepared by drop-casting from various blend compositions in *o*-DCB onto a PEDOT:PSS/glass substrate. Floating the film onto deionized water and allowing it to dry in an oven for complete removal of water vapors helps to collect enough dried blend film for the analysis.

DSC thermograms were measured using a DSC Q100 apparatus from TA Instruments. Samples were first heated from 0 to 300 °C, cooled from 300 to 0 °C, heated again from 0 to 300 °C, and then characterized on a second heating run. All experiments were performed at a rate of 10 °C $\cdot \text{min}^{-1}$.

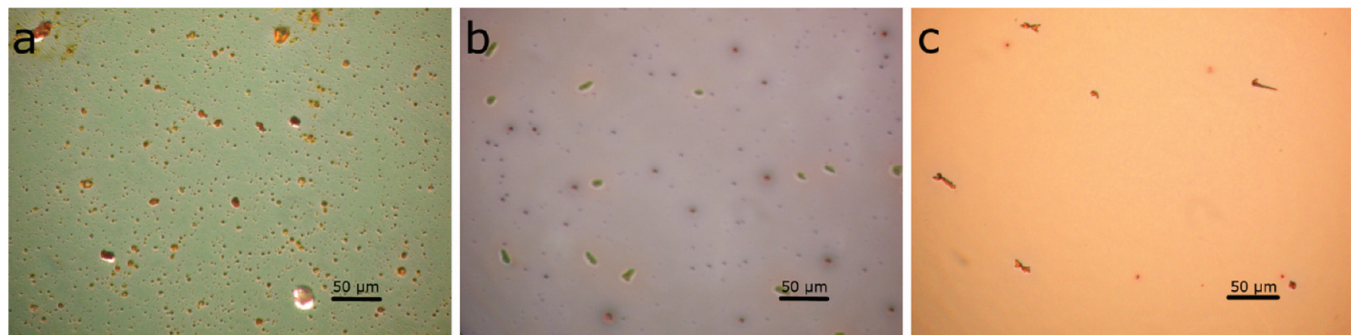


Figure 1. Optical microscopy images ($\times 40$) of P3HT:PCBM 1:1 thin films spin-coated using different molecular weight P3HTs after annealing at $180\text{ }^{\circ}\text{C}$ for 20 min: 9.6 kg/mol (a), 25 kg/mol (b), and 60 kg/mol (c).

Photovoltaic Measurements. For device fabrication a standard configuration was used, i.e., glass/ITO/PEDOT:PSS/P3HT:PCBM/Al. Substrates (glass coated with ITO) were cleaned in an ultrasonic bath in acetone, ethanol, and isopropanol. After the substrate was dried and treated in UV–ozone for 15 min, a thin layer (80 nm) of PEDOT:PSS was spin-coated at 4000 rpm and dried in an oven at $110\text{ }^{\circ}\text{C}$ under a rotary pump vacuum for 1 h. The thickness of the PEDOT:PSS layer was 80 nm as measured by an Alpha-step IQ surface profiler. All procedures after PEDOT:PSS deposition were performed in an inert-atmosphere (N_2) in a glovebox (O_2 and $\text{H}_2\text{O} < 0.1\text{ ppm}$). Subsequently, the photoactive layer (P3HT:PCBM) was spin-coated on top of the PEDOT:PSS layer from an *o*-DCB solution at $50\text{ }^{\circ}\text{C}$. The thickness of the photoactive layer was typically in the range of 100–150 nm. The aluminum electrode was thermally deposited (80 nm) through a shadow mask with an average pressure of $\sim 10^{-6}\text{ mbar}$. Thermal annealing treatment was performed after aluminum electrode deposition (post annealing treatment) on a temperature-controlled hot plate at $180\text{ }^{\circ}\text{C}$ for 20 min. Devices were left to cool down to room temperature before testing. Current–voltage characteristics were recorded using a Keithley 4200 SCS, under an illumination of 100 mW/cm^2 from a KHS Solar Celltest 575 solar simulator with AM 1.5G filters. Four 8.4 mm^2 photovoltaic cells were fabricated on each $15 \times 15\text{ mm}^2$ substrate. In order to check the repeatability of the characteristics, the measurements were performed on 16 different devices.

SFM and TEM Analysis. All the thin films used for SFM and TEM observations were performed on the active layers of the actual devices in order to ensure that the observed morphologies were typical. The active layer was first observed with SFM, which does not damage the samples, followed by TEM.

SFM measurements were obtained with a Dimension Icon Atomic Force Microscope (DI-Veeco) system operated in tapping mode in air at room temperature. Commercial silicon cantilevers with typical force constants between 32.0 and $54.4\text{ N}\cdot\text{m}^{-1}$ were used. The measurements were carried out at specific positions of the sample with different scan sizes (typically 0.5, 1, and $2\text{ }\mu\text{m}$). Each scanned micrograph consists of 512 lines. Images were taken continuously with a scan rate of 1.0 Hz. Tapping mode gives a phase contrast that essentially reveals information of the hardness of solid surfaces, nanoparticles, and soft materials. The preparation of the SFM samples was performed by peeling off the aluminum electrode partially covering the active layer. SFM characterization was conducted on the areas not covered by the aluminum electrode in order to exclude any morphological damage induced by this process.

Following SFM observations, the active layer films were collected from the devices for further TEM observations. For that purpose, the devices were immersed into deionized water to dissolve PEDOT:PSS and allow the blend film to float. It was then collected and placed on a 400 square-mesh copper TEM grid (Agar Sci., Inc.). TEM images were recorded using a Hitachi H-7650 transmission electron microscope operated at 80 kV. As spatial resolution obtained under focused conditions is limited,^{41,42} images were taken under slightly defocused (i.e., phase contrast) conditions to better visualize the fibers, rods, and networks of the constituents. For example, in bright-field TEM under these particular experimental conditions, P3HT nanorods appear bright, and PCBM-rich regions appear dark because of the lower density of P3HT crystals (1.1 g/cm^3) as compared to PCBM (1.5 g/cm^3).^{25,41,43–46}

Optical Microscopy Analysis. The thin films used for transmission optical microscopy observations in order to depict the phase behavior of the blends (Figure 9) were spin-coated directly onto ITO under the same conditions as in devices. The PEDOT:PSS thin layer was here not included as it can be damaged when heated above $200\text{ }^{\circ}\text{C}$. The other optical microscopy images (Figure 1) were acquired from the actual devices.

Transmission optical microscopy observations were carried out with a Leitz Laborlux K Microscope equipped with a Moticam 2000 compact professional camera and a Mettler Toledo FP82HT hot stage. For the *in situ* heating, the sample was placed in a sample holder with a closed loop heating system. Image capturing was started when the temperature of the sample holder was ramped to $160\text{ }^{\circ}\text{C}$.

X-ray Photoelectron Spectroscopy (XPS) Measurements. XPS measurements were made using an ESCALAB 220-iXL spectrometer (Thermo-Electron, VG Company). Photoemission was stimulated by a monochromatized Al Ka radiation (1486.6 eV). An area of about 250 nm diameter was analyzed for each sample. Surveys and high-resolution spectra were recorded and then fitted with an advantage processing program provided by Thermo-Fisher Scientific.

■ RESULTS

Synthesis of P3HTs of Various Molecular Weights from 5.8 to 60 kg/mol. Five P3HTs with different molecular weights were synthesized via the Grignard metathesis route.^{38–40} The tailoring of the molecular weight was obtained by changing the ratio of 1,3-bis(diphenylphosphino)propane nickel(II) dichloride with respect to the monomer in the starting mixture

Table 1. Macromolecular Characteristics of the Studied P3HTs

P3HT	P3HT-5.8k	P3HT-9.6k	P3HT-25k	P3HT-40k	P3HT-60k	P3HT-105k ^c
M_n^a (kg/mol)	5.8	9.6	25	40	60	105
dispersity ^a	1.6	1.3	1.1	1.4	1.4	1.9
regioregularity (%) ^b	89	92	96	98	99	98

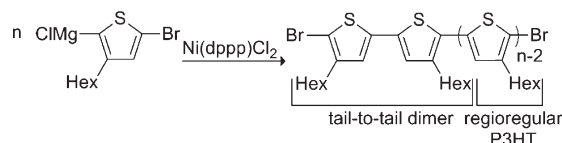
^a M_n determined by SEC with polystyrene standards in THF at 40 °C. ^b Determined by ¹H NMR using CDCl₃ as solvent. ^c Commercial P3HT.

(see Experimental Section). Their molecular weight and dispersity were determined by SEC using polystyrene homopolymers as standards (polystyrene standards overestimate the real molecular weight by a factor between 1.2 and 2.3),⁴⁷ and the regioregularity defined as the percentage of head-to-tail monomer coupling was determined by ¹H NMR. Finally, a commercial P3HT with a high molecular weight was used to complete the study.

The macromolecular characteristics of the different P3HT samples are listed in Table 1. For the synthesized P3HTs, the regioregularity increases with molecular weight. Grignard metathesis induces a tail-to-tail coupling of the two first monomer units as shown in Scheme 1.⁴⁸ Thus, in each chain, there is at least one sequence irregularity. Consequently, the smaller the number of monomer units in one chain, the smaller the regioregularity. It is noteworthy that the dispersions of all the synthesized P3HTs were quite low, ranging from 1.1 to 1.6, as compared to the commercial P3HT-105k with a dispersity of 1.9.

The main thermal characteristics of the different P3HTs were determined by DSC measurements and are reported in Table 2. The degree of crystallinity is here defined as the ratio between the measured enthalpy of melting and the enthalpy of melting of a perfect polymer (ΔH_u^0). For P3HT, ΔH_u^0 has been calculated by Malik et al. from the melting point depression in the polymer–diluents system and was determined as $\Delta H_u^0 = 99 \text{ J/g}$.⁴⁹ P3HT-5.8k presents the lowest degree of crystallinity because it has the poorest regioregularity (89%, Table 1). Indeed, high regioregularity implies a better packing of the P3HT chains⁵⁰ and thus an improved degree of crystallinity. For the other P3HTs, the regioregularity is comparable, and it is noteworthy that the higher the molecular weight of P3HT, the lower its crystallinity and the higher its melting point.

Influence of the Molecular Weight of P3HT. The annealing time and temperature were fixed for all the experiments at 20 min and 180 °C, respectively, as these annealing parameters gave the best photovoltaic performance. Optical microscopy images as well as SFM and TEM images of films of P3HT-9.6k, P3HT-25k, and P3HT-60k in blend with PCBM (1:1) annealed at 180 °C are presented in Figures 1, 2, and 3, respectively. A dramatic difference in the PCBM agglomeration was noticed in the optical microscopy images (Figure 1): many microscopic PCBM agglomerates are present in the low molecular weight P3HT (P3HT-9.6k) films, while for higher molecular weight P3HT films (P3HT-40k and P3HT-60k) fewer and thinner PCBM agglomerates are observed. The SFM image (Figure 2a) shows poor nanoscale organization between P3HT-9.6k and PCBM, as shown by large areas composed of grains corresponding to highly crystalline low molecular weight P3HT and PCBM agglomerates (bright areas) surrounded by soft regions (amorphous P3HT, dark areas). By contrast, Figure 2b (P3HT-25k) presents a well-defined fibrillar structure. Figure 2c shows the corresponding SFM image for P3HT-60k, which exhibits a much more homogeneous structure relative to Figure 2a, suggesting an intimate mixing between P3HT and PCBM. With the increase of the

Scheme 1. Polymerization of 3-Hexylthiophene via the Grignard Metathesis Route

molecular weight, TEM images (Figure 3) show smaller domains of P3HT and PCBM, which should lead to better exciton dissociation and to higher short circuit currents (j_{sc}) and fill factors (FF) in the resulting devices. Figure 3a especially shows isolated areas of P3HT-9.6k without interconnection to each other, whereas Figure 3c shows a “salt and pepper” pattern inherent to the lack of contrast obtained with defocused TEM on this particular system allowing us to conclude the overall mixing between the P3HT-60k and PCBM domains without large PCBM agglomerates or P3HT crystallites. This good homogeneity in the repartition of P3HT and PCBM is required for a more efficient transport of charge carriers through a percolated system.

While SFM only reveals the surface mesostructure, TEM enables knowledge of the bulk organization (Figure 4), and thus the combination of these two techniques provide complementary information on the surface and bulk components in the P3HT/PCBM mesostructure. Good agreement between the TEM and SFM for P3HT-9.6k and P3HT-60k images are noted: in Figures 2a and 3a (P3HT-9.6k) we show large areas of crystalline or agglomerated materials and a rather broken morphology, while Figures 2c and 3c (P3HT-60k) present an homogeneous mixing of P3HT and PCBM as suggested by the “salt and pepper” pattern without clear features. However, for P3HT-25k, SFM and TEM characterizations do not show such agreement, suggesting a preferential segregation at the aluminum electrode side of the device of one of the film components (see Discussion).

For all the P3HTs (from P3HT-5.8k to P3HT-105k), the photovoltaic characteristics for a 1:1 P3HT:PCBM blend after 20 min of annealing at 180 °C was measured and reported in Figure 5. j_{sc} is connected to the lifetime and mobility of the charge carriers in the mixture of the materials and, thus, is strongly linked to the morphology of the active layer. The FF results from the competition between charge transport and charge recombination.^{51,52} In order to increase the FF, the morphology of the active layer has to be suitable for charge transport, i.e., a nanostructured bicontinuous phase. The open circuit voltage (V_{oc}) is related to the energy gap between the highest occupied molecular orbital (HOMO) of the electron donor material and the lowest unoccupied molecular orbital (LUMO) of the electron acceptor material.^{53,54} The values of V_{oc} and the FF also depend on the quality of the interfaces between the electrodes and the active layer.^{52,55} j_{sc} , FF, and PCE increase with the molecular weight up to 60 kg/mol and then reach a plateau for higher molecular weights. The increase of the j_{sc} and

Table 2. Melting and Crystallization Temperatures, Degree of Crystallinity for the Different P3HTs

P3HT	P3HT-5.8k	P3HT-9.6k	P3HT-25k	P3HT-40k	P3HT-60k	P3HT-105k
melting temperature (°C)	204	217	233	234	234	351
crystallization temperature (°C)	178	190	206	202	199	192
degree of crystallinity (%) ^a	7.2	18.0	14.7	12.2	10.9	9.9

^aDefined as the ratio between the measured enthalpy of melting and the enthalpy of melting of a perfect polymer.

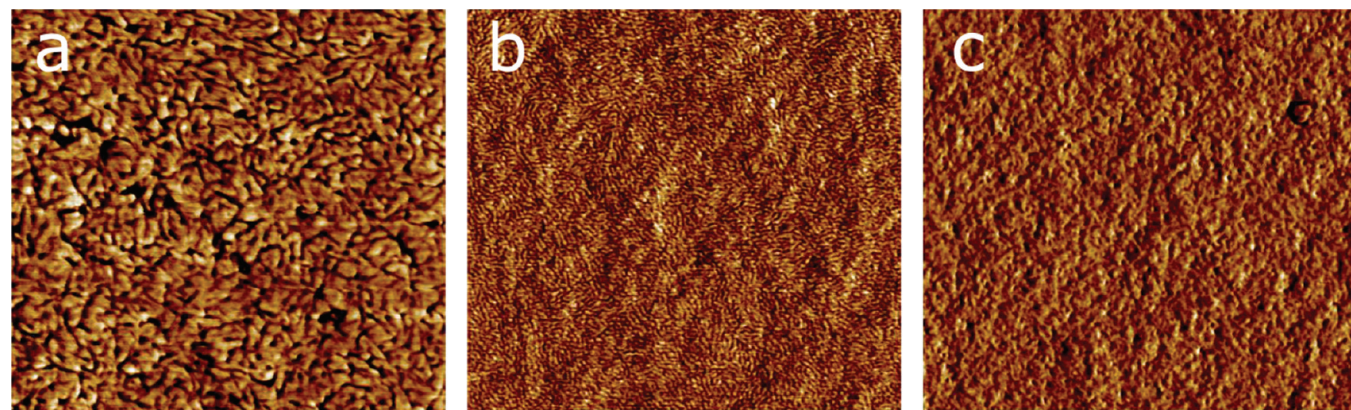


Figure 2. SFM phase images of P3HT:PCBM 1:1 thin films for different molecular weight P3HTs: 9.6 kg/mol (a), 25 kg/mol (b), and 60 kg/mol (c). The images are 2 $\mu\text{m} \times 2 \mu\text{m}$ scans.

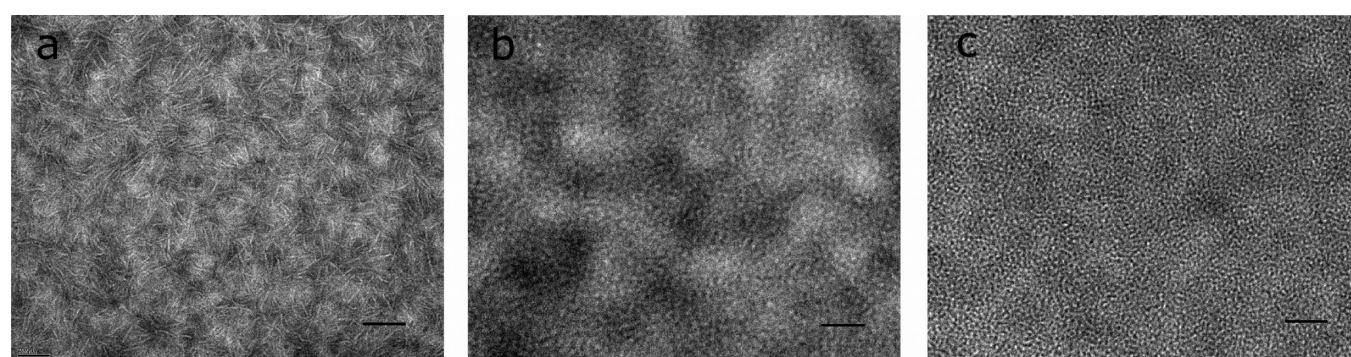


Figure 3. TEM images of P3HT:PCBM thin films 1:1 for different molecular weight P3HTs: 9.6 kg/mol (a), 25 kg/mol (b), and 60 kg/mol (c). The scale bar represents 200 nm.

the FF with the molecular weight is in agreement with the improvement of the percolated morphology with the increasing molecular weight as observed on SFM and TEM images (Figures 2 and 3). This is consistent with the fact that a nanosized bicontinuous structure between a donor and an acceptor is the most appropriate candidate to both dissociate the exciton and conduct the charges to the electrodes.^{3–5} Moreover, for the two highest molecular weights, a 2.8% PCE was obtained.

Except for P3HT-9.6k, which has a low open circuit voltage, v_{oc} decreases with increasing molecular weight. This can be explained by both the raising of the HOMO level of the P3HT with the molecular weight and by the increase in the dark saturation current, which leads to a decrease in v_{oc} ^{56–61} (see Discussion).

For the P3HT-60k and P3HT-105k, all the photovoltaic parameters seem to reach a plateau. At this molecular weight threshold, phase separation is complete, providing well-defined interfaces for dissociation. The length scale of the phase separation (as shown in Figures 2c and 3c for P3HT-60k and Figure S2,

Supporting Information, for P3HT-105k) does not change, and thus the morphology is optimized for photovoltaic process.

In summary, the photovoltaic parameters increase with P3HT molecular weight. At a composition of P3HT:PCBM 1:1, SFM and TEM images confirm that P3HT-60k presents an improved morphology for exciton dissociation and bipolar charge transport relative to the lower M_n P3HTs.

Phase Behavior. The phase behavior of P3HT-9.6k, P3HT-25k, and P3HT-60k blended with PCBM was investigated. The phase diagrams (temperature/composition) for all P3HT:PCBM binary blends were obtained using DSC as shown in Figure 6. A eutectic system was found on each phase diagram between 50 and 65 wt % of P3HT depending on the P3HT molecular weight (Figure 7). The P3HT eutectic composition c_e is defined as the composition that exhibits the lowest melting point for the homogeneous mixture of the two components. By heating the two components at the composition c_e above the eutectic temperature T_e and then by cooling them down, they simultaneously solidify in a finely intermixed (cocontinuous)

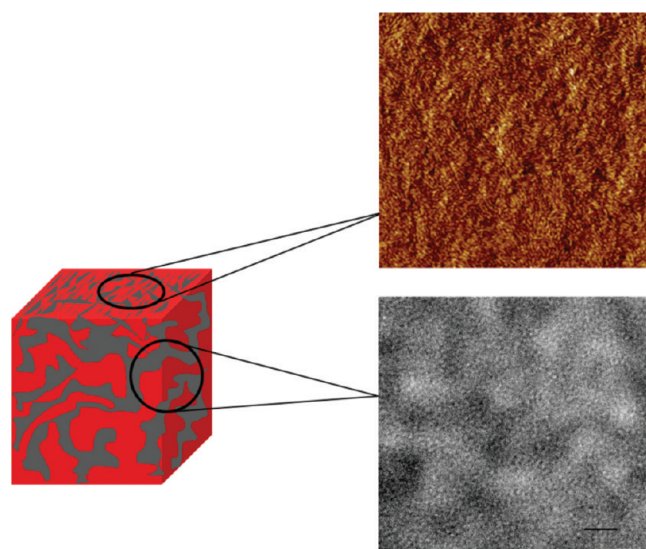


Figure 4. Schematic representation of the preferential segregation of the active layer for P3HT-25k. Top: SFM image of P3HT-25k:PCBM 1:1 (Figure 2b); bottom: TEM image of P3HT-25k:PCBM 1:1 (Figure 3b). In red: P3HT; in gray: PCBM.

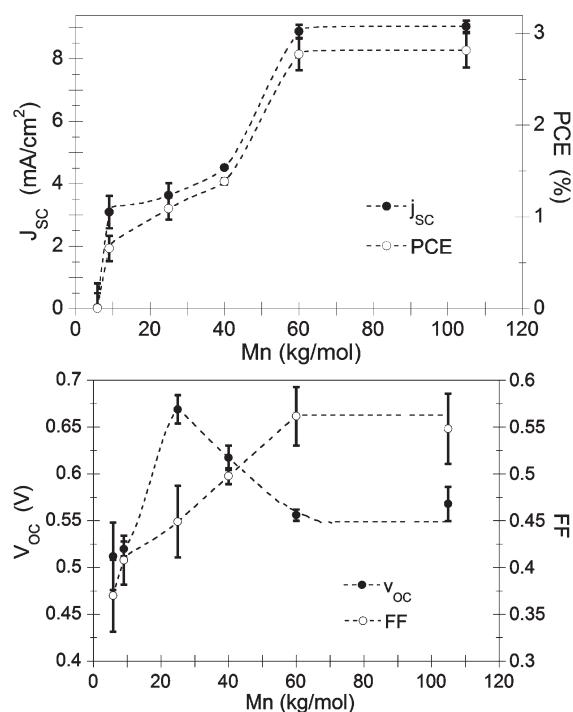


Figure 5. Photovoltaic performance after 20 min of post annealing at 180°C for 1:1 P3HT:PCBM blends as a function of the P3HT molecular weight. The vertical bar on each point is the standard deviation measured on 16 different photovoltaic cells.

solid structures. For hypo- or hyper-eutectic P3HT compositions (hypo-eutectic $c < c_e$ and hyper-eutectic $c > c_e$), when the mixture is heated at a temperature above the liquidus line and cooled down, primary crystals of the majority component are formed, and then the two components solidify simultaneously at a temperature below T_e , resulting in a structure with the majority of the crystalline component surrounded by a matrix of both

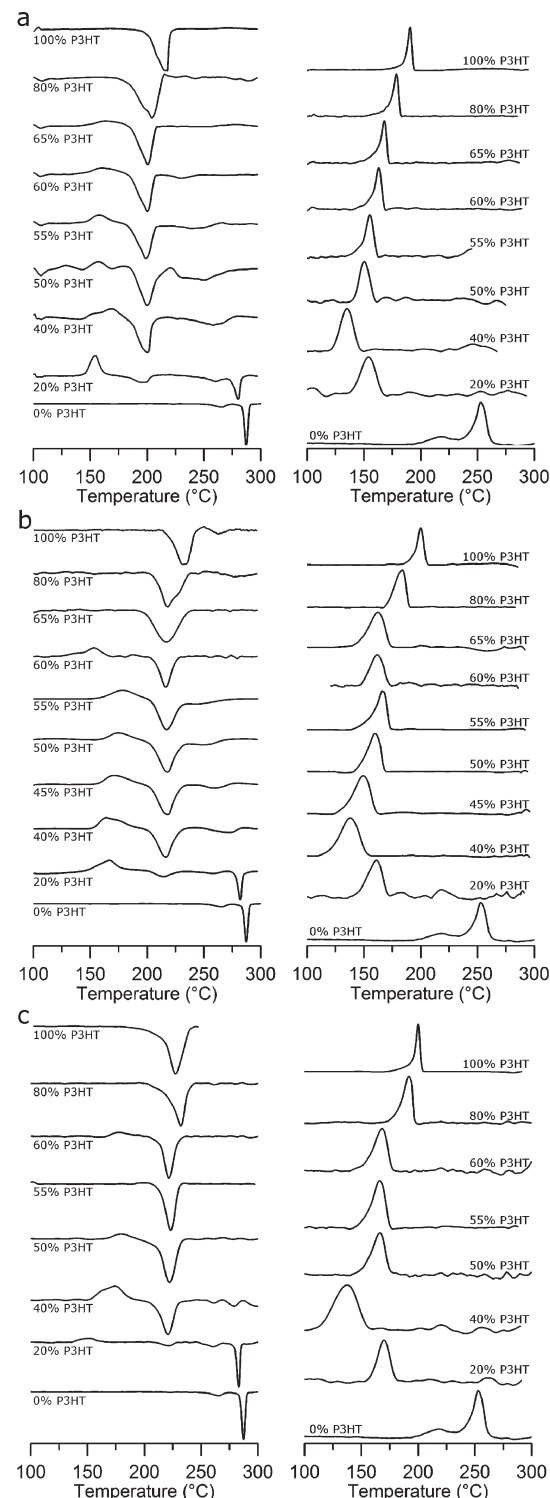


Figure 6. DSC thermograms of P3HT:PCBM blend films for different compositions of P3HT and different P3HT molecular weights: 9.6 kg/mol (a), 25 kg/mol (b), and 60 kg/mol (c). On the right, the melting part from 100 to 300 °C; on the left, the crystallization part from 300 to 100 °C.

components.³⁶ Interestingly, the introduction of PCBM in a blend with P3HT leads to a decrease of the binary system crystallization temperature since the inclusion of PCBM reduces the size of the P3HT crystallites and thus the P3HT melting point.⁶² It is noteworthy that the optimal (from a photovoltaic

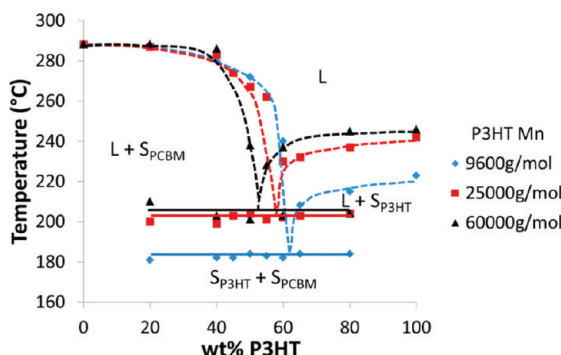


Figure 7. Overlay of phase diagrams between different molecular weight P3HTs and PCBM obtained on the basis of the DSC thermograms (Figure 6). Solid lines: solidus lines; dash lines: liquidus lines. Solidus lines correspond to the appearance of the first drop of liquid (i.e., the temperature at the beginning of the first peak in the melting part). Liquidus lines correspond to the temperature at the end of the majority component peak in the melting part. L: liquid part; S_{PCBM}: solid solution of PCBM; S_{P3HT}: solid solution of P3HT.

point of view) annealing temperature ($180\text{ }^{\circ}\text{C}$) experimentally determined for the 50 wt % binary system is located between the crystallization and the melting temperatures (Figure 6). This particular annealing temperature causes an increase in the P3HT crystallinity by inducing the crystallization of a larger part of the amorphous P3HT without the melting of the P3HT crystals.

The phase diagrams deduced from the DSC measurements for P3HT-9.6k, P3HT-25k, and P3HT-60k blended with PCBM are depicted in Figure 7. The eutectic point relative to the P3HT composition is located between 60 and 65 wt %, 55 and 60 wt %, and 50 and 55 wt % for P3HT-9.6k, P3HT-25k, and P3HT-60k respectively. A shift in the eutectic composition is observed; the lower the molecular weight, the higher the eutectic composition of P3HT. This trend was also confirmed by comparing the photovoltaic performance of these P3HTs as shown in Figure 8. For the blend made with P3HT-9.6k, the j_{sc} and PCE maximum corresponds to a blend ratio composed of 65 wt % of P3HT, whereas it is 60 wt % for P3HT-60k. For low molecular weight P3HTs, more P3HT is needed to achieve a better nanoscale bicontinuous organization of the active layer and so to achieve efficient charge transport. As observed previously (Figure 5), the difference PCE between the P3HTs of various molecular weights is mainly due to the increase of j_{sc} and FF with the molecular weight of the P3HT, whatever the composition of the active layer.

Thin films with different compositions of P3HT:PCBM were studied *in situ* by optical microscopy during heating (Figure 9). For a hypo-eutectic composition, microscopic PCBM agglomerates appear at $180\text{ }^{\circ}\text{C}$ and then melt at temperatures around $240\text{--}280\text{ }^{\circ}\text{C}$. These PCBM agglomerates only appear when there is at least 20 wt % of P3HT in the film, which supports the idea that the crystallization of the P3HT induces the agglomeration of the PCBM. The appearance and disappearance of the PCBM agglomerates correspond to the solidus lines and the liquidus lines from the phase diagrams presented in Figure 7. PCBM crystallization is confirmed by the presence of exothermic peaks due to the PCBM crystallization apparent on DSC thermograms upon heating around $180\text{ }^{\circ}\text{C}$ for hypo-eutectic composition.

DISCUSSION

Influence of the molecular weight. In this work we correlate the morphological changes induced by different P3HT molecular weights in P3HT/PCBM blends with their photovoltaic properties. The micrographs obtained by SFM and TEM characterization, as shown in Figures 2 and Figure 3, reveal a dramatic P3HT molecular weight dependence on the morphology of P3HT/PCBM blends. The disrupted (i.e., not interconnected) structure observed with both SFM and TEM for P3HT-9.6k (Figures 2a and 3a) evolves, as the P3HT molecular weight increases, to more homogeneous structures with smaller domain sizes (Figure 3b,c). The difference between the SFM and TEM images for P3HT-25k (Figures 2b and 3b) suggests a preferential segregation of one of the film components at the aluminum electrode side. Preferential segregation between P3HT and PCBM leading to a depletion of PCBM at the aluminum electrode has already been reported for either freshly cast films (before annealing)^{22,63,64} and annealed films.⁶⁵ Furthermore, the SFM image (Figure 2b) of the surface between the active layer and aluminum, shows a fibrillar structure close to the one of a pristine P3HT thin film (images available in Supporting Information Figure S1).^{30,66,67} We therefore believe that a preferential segregation of P3HT-25k to the aluminum electrode leads to a depletion of PCBM at this interface. This conclusion is also supported by XPS data, which reveals roughly the same composition for the blend with P3HT as for a pristine P3HT thin layer (see Supporting Information Table S1). We ascribe such preferential segregation to the low dispersity of P3HT-25k (see Table 1). Indeed an enhanced miscibility of two components in the blend is expected with increased dispersity.^{68–70} The smallest chains of a polydisperse polymer are able to migrate more easily to the interface between the two constituents and thus decrease the interfacial tension between the two polymers. As a consequence, with a monodisperse polymer such as P3HT-25k, the P3HT:PCBM blend has a larger tendency to phase segregate, leading to a segregation of the P3HT at the top interface.⁶⁸

As shown in Figure 5, FF, PCE, and j_{sc} increase with increasing P3HT molecular weight up to 60 kg/mol except for v_{oc} , which exhibits a maximum for P3HT-25k and decreases for higher molecular weight P3HTs. This v_{oc} evolution can be attributed to two distinct phenomena. The open circuit voltage usually correlates to the energy difference between the HOMO level of the donor and the LUMO level of the acceptor.^{53,54} It has been observed that the HOMO energy level of P3HT increases with molecular weight,^{58,59} which causes a reduction in v_{oc} from P3HT-25k to P3HT-105k. However, v_{oc} is also dependent on the reverse dark saturation current j_0 measured from the current–voltage characteristics of the photovoltaic cells,^{56,57,60,61} and we observe that the reverse saturation dark current for P3HT-25k-based devices is strongly reduced compared to the other devices following⁵⁷

$$v_{oc} = \frac{kT}{q} \ln \left(\frac{j_{sc}}{j_0} + 1 \right)$$

where k is the Boltzmann constant, T is the absolute room temperature, and q is the elementary electron charge.

For higher molecular weight P3HTs, the saturation dark currents are in the same range, and the lowering of v_{oc} is mainly related to the decrease of the HOMO level of the P3HTs. The reason for the low reverse saturation dark current for P3HT-25k

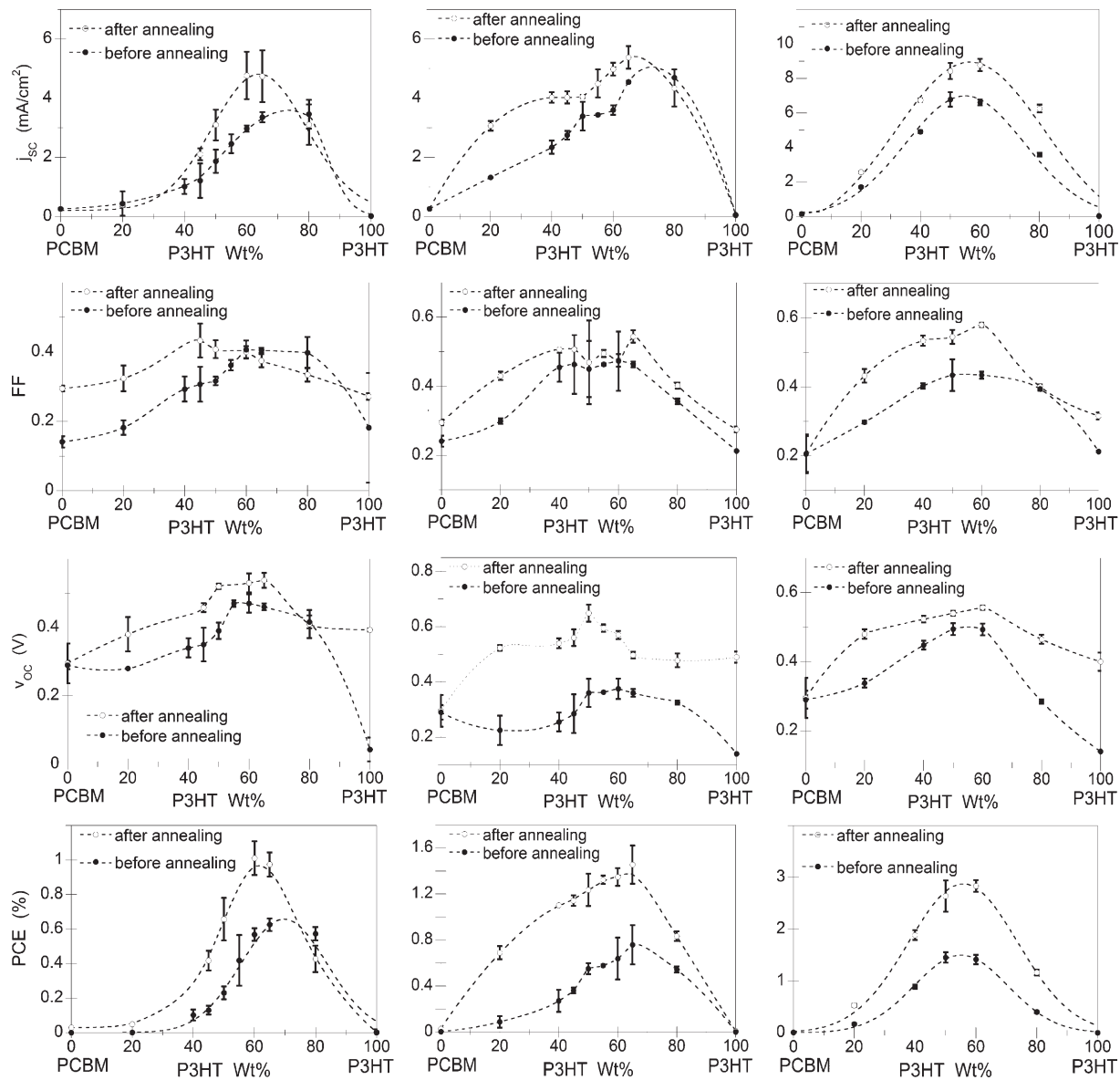


Figure 8. Photovoltaic performance of photovoltaic cells P3HT:PCBM thin films with different amounts of P3HT for different molecular weights of P3HT before and after annealing. From left to right, 9.6 kg/mol, 25 kg/mol, and 60 kg/mol. The vertical bar on each point is the standard deviation measured on 16 different solar diodes.

is probably related to the observed P3HT-rich layer that has been detected at the aluminum side of the device. Such a decrease has previously been suggested to be due to the presence of a high carrier-injection barrier at reverse bias.⁷¹ It is thus possible to conclude that the P3HT-rich layer acts as a high carrier-injection barrier, which reduces the saturation dark current and thus increases the v_{oc} (Figure 10).

Apart from the v_{oc} , the other photovoltaic parameters (j_{sc} , FF, and PCE) increase with increasing P3HT molecular weight up to 60 kg/mol. A possible explanation is linked to the regioregularity, which increases with M_n , leading to a better packing of the chains through the formation of extended lamellae structure with improved π -stacking.⁷² Second, low M_n P3HTs are very crystalline (apart from P3HT-5.8 k, Table 2) and form small rigid nanorod crystals dispersed in a PCBM matrix that are poorly interconnected to each other (Figure 3a). As a consequence, hole transport in the active layer to the ITO electrode, mainly assisted

by the P3HT, is not efficient, which results in the observed poor performance. Higher molecular weight polymers exhibit a higher content of amorphous P3HT (Table 2) enabling the connection between the different crystalline parts leading to a co-continuous morphology (Figure 3b) and allowing a more efficient charge transport through the volume of the film.^{28,29,31,43}

At the macroscopic scale, the appearance of numerous PCBM agglomerates after annealing for P3HT-9.6k (Figure 1a) is due to the annealing process enabling PCBM diffusion over short distances¹⁵ leading to the agglomerate formation. P3HT and PCBM are only compatible in the amorphous state, and enhanced P3HT crystallization during annealing ejects the PCBM, which induces its agglomeration.¹⁶ For higher molecular weight P3HTs, the longer chains slow down the diffusion of PCBM because of the higher ratio of entanglements of the chains,⁷³ and few PCBM microscopic agglomerates are observed after annealing (Figure 1b,c).

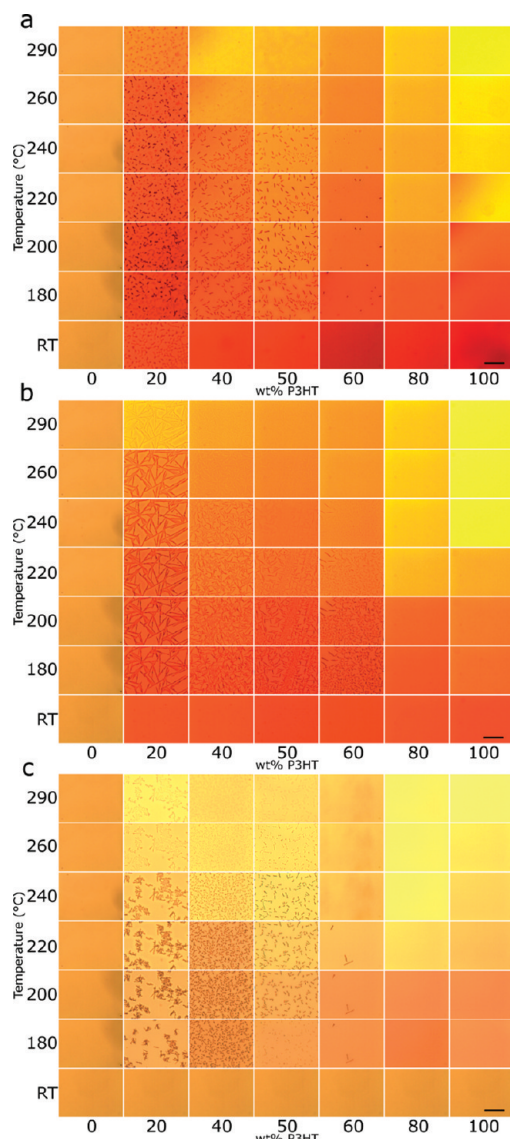


Figure 9. Optical microscopy images ($\times 40$) of P3HT:PCBM thin films while heating with different amounts of P3HT and different P3HT molecular weights: 9.6 kg/mol (a), 25 kg/mol (b), and 60 kg/mol (c). The scale bar represents 50 μm .

In summary, for a P3HT:PCBM 1:1 system, the photovoltaic performance increases with the P3HT molecular weight. The poor performance observed for low molecular weight P3HTs is mainly due to their crystallization behavior: as they form isolated crystalline nanorods, a higher amount of P3HT compared to PCBM is needed to create connections between the different P3HT domains. The establishment of the phase diagrams between P3HT and PCBM is necessary to determine the optimum ratio of the two compounds depending on the P3HT molecular weight.

Influence of the Bulk Heterojunction Composition. Depending on the P3HT molecular weight, a shift in the composition of the eutectic system is observed in the phase diagrams between P3HT and PCBM (Figure 7). Meanwhile the maximum photovoltaic performance is obtained for the eutectic composition (Figure 8). The crystallization behavior also explains these observed shifts in composition. Indeed, low molecular weight

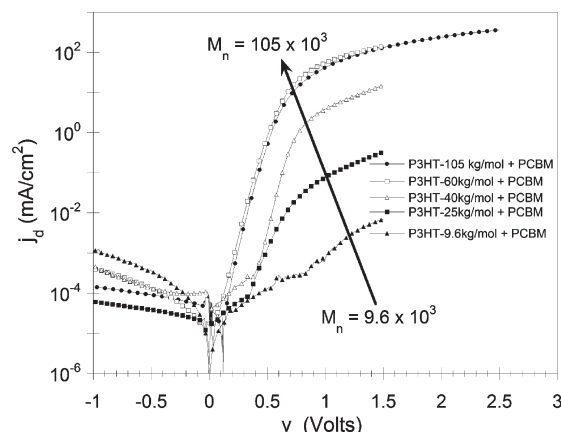


Figure 10. Dark current (j_d) as a function of the voltage (v) of P3HT:PCBM blend films for different P3HT molecular weights.

P3HTs are very crystalline and form rigid crystal nanorods dispersed in a PCBM matrix that are poorly interconnected to each other. Thus, compared to higher M_n P3HT, a larger amount of low molecular weight P3HT helps to achieve a bicontinuous solid structure leading to the eutectic system.

Comparing the photovoltaic performance before and after annealing (Figure 8), j_{sc} is shifted toward lower P3HT content for low molecular weights. Notably, for P3HT-9.6k, the maximum in j_{sc} is around 80 wt % of P3HT before annealing, whereas after annealing, it is around 65 wt % P3HT. Indeed the annealing process allows the PCBM to diffuse through the film to form microscale agglomerates, which are clearly visible in Figure 1 or Figure 9. As a consequence, there is less PCBM left in the active domains around these agglomerates, which yields a lower amount of P3HT to achieve a co-continuous structure after (rather than before) annealing. This shift in composition is not observed for the high molecular weight P3HT-60k. Indeed, due to their higher concentration of entanglements, high molecular weight P3HTs inhibit significant PCBM diffusion and thus the formation of microscale agglomerates. Consequently, for high molecular weight P3HTs, the composition for the best photovoltaic performance is largely independent of whether or not the active layer has been annealed.

CONCLUSION

A systematic approach to the study of the binary system of P3HT and PCBM has been proposed through the mapping of the binary P3HT:PCBM blend phase diagram. This approach has allowed us to determine the correlations between the P3HT molecular weight and dispersity, the active layer morphology, and the photovoltaic performance. The establishment of the P3HT:PCBM phase diagrams provides a better understanding of the interdependences between P3HT crystallization, the diffusion of PCBM to form microscale agglomerates, and more generally, the phase separation mechanisms occurring during the annealing process. We showed that the P3HT macromolecular characteristics are determining factors for the morphology and the photovoltaic performance and that the optimal ratios of P3HT and PCBM in the active layer are inherent to the P3HT molecular weight. Moreover, we have demonstrated that the maximum photovoltaic characteristics are obtained for the eutectic composition of the active layer.

■ ASSOCIATED CONTENT

S Supporting Information. Pristine P3HT SFM images, XPS data, SFM, and TEM images of P3HT-105k:PCBM blend. This information is available free of charge via the Internet at <http://pubs.acs.org>.

■ AUTHOR INFORMATION

Corresponding Author

*E-mail: gfeury@enscbp.fr (G.F.); hadzii@enscbp.fr (G.H.).

Permanent Addresses

University of Sheffield, Department of Physics and Astronomy, Hicks Building, Hounsfield Road, Sheffield S3 7RH, United Kingdom.

■ ACKNOWLEDGMENT

The authors gratefully acknowledge financial support from Arkema and the Region Aquitaine through the chair for "Advanced Functional Materials for the Emerging Information, Communication and Energy Technologies". Arkema and the Region Aquitaine are thanked for funding C.N. and C.R., respectively. Portions of this work were carried out at the Bordeaux Imaging Center, and we also thank Etienne Gontier's team for helpful discussions on the TEM characterizations. We thank Christine Labrugère from Institut de Chimie de la Matière Condensée de Bordeaux for XPS measurements. M.G. is grateful to the Université Bordeaux for a visiting professorship.

■ REFERENCES

- (1) Ma, W.; Yang, C.; Gong, X.; Lee, K.; Heeger, A. J. *Adv. Funct. Mater.* **2005**, *15*, 1617–1622.
- (2) Peet, J.; Senatore, M. L.; Heeger, A. J.; Bazan, G. C. *Adv. Mater.* **2009**, *21*, 1521–1527.
- (3) Yang, X.; Loos, J.; Veenstra, S. C.; Verhees, W. J. H.; Wienk, M. M.; Kroon, J. M.; Michels, M. A. J.; Janssen, R. A. J. *Nano Lett.* **2005**, *5*, 579–583.
- (4) Halls, J. J. M.; Walsh, C. A.; Greenham, N. C.; Marseglia, E. A.; Friend, R. H.; Moratti, S. C.; Holmes, A. B. *Nature* **1995**, *376*, 498–500.
- (5) Yu, G.; Gao, J.; Hummelen, J. C.; Wudl, F.; Heeger, A. J. *Science* **1995**, *270*, 1789–1791.
- (6) Veenstra, S. C.; Malliaras, G. G.; Brouwer, H. J.; Esselink, F. J.; Krasnikov, V. V.; van Hutten, P. F.; Wildeman, J.; Jonkman, H. T.; Sawatzky, G. A.; Hadzioannou, G. *Synth. Met.* **1997**, *84*, 971–972.
- (7) Ouali, L.; Krasnikov, V. V.; Stalmach, U.; Hadzioannou, G. *Adv. Mater.* **1999**, *11*, 1515–1518.
- (8) Yin, W.; Dadmun, M. *ACS Nano* **2011**, *5*, 4756–4768.
- (9) Chen, W.; Xu, T.; He, F.; Wang, W.; Wang, C.; Strzalka, J.; Liu, Y.; Wen, J.; Miller, D. J.; Chen, J.; Hong, K.; Yu, L.; Darling, S. B. *Nano Lett.* **2011**, null–null.
- (10) Shin, M.; Kim, H.; Park, J.; Nam, S.; Heo, K.; Ree, M.; Ha, C. S.; Kim, Y. *Adv. Funct. Mater.* **2010**, *20*, 748–754.
- (11) Reyes-Reyes, M.; Kim, K.; Carroll, D. L. *Appl. Phys. Lett.* **2005**, *87*, 1–3.
- (12) Erb, T.; Zhokhavets, U.; Gobsch, G.; Raleva, S.; Stühn, B.; Schilinsky, P.; Waldau, C.; Brabec, C. *Adv. Funct. Mater.* **2005**, *15*, 1193–1196.
- (13) Hwang, I.-W.; Moses, D.; Heeger, A. J. *J. Phys. Chem. C* **2008**, *112*, 4350–4354.
- (14) van Bavel, S. S.; Bärenklau, M.; De With, G.; Hoppe, H.; Loos, J. *Adv. Funct. Mater.* **2010**, *20*, 1458–1463.
- (15) Watts, B.; Belcher, W. J.; Thomsen, L.; Ade, H.; Dastoor, P. C. *Macromolecules* **2009**, *42*, 8392–8397.
- (16) Bertho, S.; Janssen, G.; Cleij, T. J.; Conings, B.; Moons, W.; Gadisa, A.; D'Haen, J.; Goovaerts, E.; Lutsen, L.; Manca, J.; Vanderzande, D. *Sol. Energy Mater. Sol. Cells* **2008**, *92*, 753–760.
- (17) Nieuwendaal, R. C.; Snyder, C. R.; Kline, R. J.; Lin, E. K.; VanderHart, D. L.; DeLongchamp, D. M. *Chem. Mater.* **2010**, *22*, 2930–2936.
- (18) Savenije, T.; Kroese, J.; Yang, X.; Loos, J. *Adv. Funct. Mater.* **2005**, *15*, 1260–1266.
- (19) Swinnen, A.; Haeldermans, I.; vande Ven, M.; D'Haen, J.; Vanhooyland, G.; Aresu, S.; D'Olieslaeger, M.; Manca, J. *Adv. Funct. Mater.* **2006**, *16*, 760–765.
- (20) Swinnen, A.; Haeldermans, I.; Vanlaeke, P.; D'Haen, J.; Poortmans, J.; D'Olieslaeger, M.; Manca, J. *V. Eur. Phys. J. Appl. Phys.* **2006**, *36*, 251–256.
- (21) Kiel, J. W.; Eberle, A. P. R.; Mackay, M. E. *Phys. Rev. Lett.* **2010**, *105*, 168701.
- (22) Chen, D.; Nakahara, A.; Wei, D.; Nordlund, D.; Russell, T. P. *Nano Lett.* **2010**, *11*, 561–567.
- (23) Treat, N. D.; Brady, M. A.; Smith, G.; Toney, M. F.; Kramer, E. J.; Hawker, C. J.; Chabinyc, M. L. *Adv. Energy Mater.* **2011**, *1*, 82–89.
- (24) Sary, N.; Richard, F.; Brochon, C.; Leclerc, N.; Lévéque, P.; Audinot, J.-N.; Berson, S.; Heiser, T.; Hadzioannou, G.; Mezzenga, R. *Adv. Mater.* **2010**, *22*, 763–768.
- (25) Vaynzof, Y.; Kabra, D.; Zhao, L.; Chua, L. L.; Steiner, U.; Friend, R. H. *ACS Nano* **2011**, *5*, 329–336.
- (26) Chen, L.-M.; Hong, Z.; Li, G.; Yang, Y. *Adv. Mater.* **2009**, *21*, 1434–1449.
- (27) Chirvase, D.; Parisi, J.; Hummelen, J.; Dyakonov, V. *Nanotechnology* **2004**, *15*, 1317.
- (28) Brinkmann, M.; Rannou, P. *Adv. Funct. Mater.* **2007**, *17*, 101–108.
- (29) Brinkmann, M.; Rannou, P. *Macromolecules* **2009**, *42*, 1125–1130.
- (30) Dante, M.; Peet, J.; Nguyen, T.-Q. *J. Phys. Chem. C* **2008**, *112*, 7241–7249.
- (31) Kline, R. J.; McGehee, M. D.; Kadnikova, E. N.; Liu, J.; Fréchet, J. M. J.; Toney, M. F. *Macromolecules* **2005**, *38*, 3312–3319.
- (32) Virkar, A. A.; Mannsfeld, S.; Bao, Z.; Stingelin, N. *Adv. Mater.* **2010**, *22*, 3857–3875.
- (33) Dang, M. T.; Hirsch, L.; Wantz, G. *Adv. Mater.* **2011**, DOI: 10.1002/adma.201100792.
- (34) Kim, Y.; Choulis, S.; Nelson, J.; Bradley, D.; Cook, S.; Durrant, J. J. *Mater. Sci.* **2005**, *40*, 1371–1376.
- (35) Zhao, J.; Swinnen, A.; Van Assche, G.; Manca, J.; Vanderzande, D.; Mele, B. V. *J. Phys. Chem. B* **2009**, *113*, 1587–1591.
- (36) Müller, C.; Ferenczi, T. A. M.; Campoy-Quiles, M.; Frost, J. M.; Bradley, D. D. C.; Smith, P.; Stingelin-Stutzmann, N.; Nelson, J. *Adv. Mater.* **2008**, *20*, 3510–3515.
- (37) Urien, M.; Erothu, H.; Cloutet, E.; Hiorns, R. C.; Vignau, L.; Cramail, H. *Macromolecules* **2008**, *41*, 7033–7040.
- (38) Jeffries-EL, M.; Sauvé, G.; McCullough, R. D. *Adv. Mater.* **2004**, *16*, 1017–1019.
- (39) Loewe, R. S.; Khersonsky, S. M.; McCullough, R. D. *Adv. Mater.* **1999**, *11*, 250–253.
- (40) Yokoyama, A.; Miyakoshi, R.; Yokozawa, T. *Macromolecules* **2004**, *37*, 1169–1171.
- (41) Moon, J. S.; Lee, J. K.; Cho, S.; Byun, J.; Heeger, A. J. *Nano Lett.* **2008**, *9*, 230–234.
- (42) Handlin, D. L.; Thomas, E. L. *Macromolecules* **1983**, *16*, 1514–1525.
- (43) Ma, W.; Kim, J. Y.; Lee, K.; Heeger, A. J. *Macromol. Rapid Commun.* **2007**, *28*, 1776–1780.
- (44) Moon, J. S.; Takacs, C. J.; Sun, Y.; Heeger, A. J. *Nano Lett.* **2011**, *11*, 1036–1039.
- (45) Xin, H.; Reid, O. G.; Ren, G.; Kim, F. S.; Ginger, D. S.; Jenekhe, S. A. *ACS Nano* **2010**, *4*, 1861–1872.
- (46) For crystalline materials and those with very little electron-density contrast, in slightly defocused mode TEM, the contrast is brought by the mass density difference.

- (47) Liu, J.; Loewe, R. S.; McCullough, R. D. *Macromolecules* **1999**, *32*, 5777–5785.
- (48) Sheina, E. E.; Liu, J.; Iovu, M. C.; Laird, D. W.; McCullough, R. D. *Macromolecules* **2004**, *37*, 3526–3528.
- (49) Malik, S.; Nandi, A. K. *J. Polym. Sci., Part B: Polym. Phys.* **2002**, *40*, 2073–2085.
- (50) Kim, Y.; Cook, S.; Tuladhar, S. M.; Chouli, S. A.; Nelson, J.; Durrant, J. R.; Bradley, D. D. C.; Giles, M.; McCulloch, I.; Ha, C.-S.; Ree, M. *Nat. Mater.* **2006**, *5*, 197–203.
- (51) Kim, M.-S.; Kim, B.-G.; Kim, J. *ACS Appl. Mater. Interfaces* **2009**, *1*, 1264–1269.
- (52) Gupta, D.; Mukhopadhyay, S.; Narayan, K. S. *Sol. Energy Mater. Sol. Cells* **2010**, *94*, 1309–1313.
- (53) Ma, H.; Yip, H.-L.; Huang, F.; Jen, A. K. Y. *Adv. Funct. Mater.* **2010**, *20*, 1371–1388.
- (54) Gadisa, A.; Svensson, M.; Andersson, M. R.; Inganas, O. *Appl. Phys. Lett.* **2004**, *84*, 1609–1611.
- (55) Li, G.; Yao, Y.; Yang, H.; Shrotriya, V.; Yang, G.; Yang, Y. *Adv. Funct. Mater.* **2007**, *17*, 1636–1644.
- (56) Potsavage, W. J. J.; Yoo, S.; Kippelen, B. *Appl. Phys. Lett.* **2008**, *93*, 193308.
- (57) Vandewal, K.; Tvingstedt, K.; Gadisa, A.; Inganas, O.; Manca, J. V. *Nat. Mater.* **2009**, *8*, 904–909.
- (58) Hoffmann, R.; Janiak, C.; Kollmar, C. *Macromolecules* **1991**, *24*, 3725–3746.
- (59) Moet, D. J. D.; Lenes, M.; Kotlarski, J. D.; Veenstra, S. C.; Sweelssen, J.; Koetse, M. M.; de Boer, B.; Blom, P. W. M. *Org. Electron.* **2009**, *10*, 1275–1281.
- (60) Li, N.; Lassiter, B. E.; Lunt, R. R.; Wei, G.; Forrest, S. R. *Appl. Phys. Lett.* **2009**, *94*, 023307.
- (61) Thakur, A. K.; Wantz, G.; Garcia-Belmonte, G.; Bisquert, J.; Hirsch, L. *Sol. Energy Mater. Sol. Cells* **2011**, *95*, 2131–2135.
- (62) Verploegen, E.; Mondal, R.; Bettinger, C. J.; Sok, S.; Toney, M. F.; Bao, Z. *Adv. Funct. Mater.* **2010**, *20*, 3519–3529.
- (63) Parnell, A. J.; Dunbar, A. D. F.; Pearson, A. J.; Staniec, P. A.; Dennison, A. J. C.; Hamamatsu, H.; Skoda, M. W. A.; Lidzey, D. G.; Jones, R. A. L. *Adv. Mater.* **2010**, *22*, 2444–2447.
- (64) McNeill, C. R.; Halls, J. J. M.; Wilson, R.; Whiting, G. L.; Berkebile, S.; Ramsey, M. G.; Friend, R. H.; Greenham, N. C. *Adv. Funct. Mater.* **2008**, *18*, 2309–2321.
- (65) Kiel, J. W.; Kirby, B. J.; Majkrzak, C. F.; Maranville, B. B.; Mackay, M. E. *Soft Matter* **2010**, *6*, 641–646.
- (66) Iovu, M. C.; Jeffries-El, M.; Zhang, R.; Kowalewski, T.; McCullough, R. D. *J. Macromol. Sci., Part A: Pure Appl. Chem.* **2006**, *43*, 1991–2000.
- (67) Verilhac, J.-M.; LeBlevennec, G.; Djurado, D.; Rieutord, F.; Chouiki, M.; Travers, J.-P.; Pron, A. *Synth. Met.* **2006**, *156*, 815–823.
- (68) Broseta, D.; Fredrickson, G. H.; Helfand, E.; Leibler, L. *Macromolecules* **1990**, *23*, 132–139.
- (69) Enders, S.; Hinrichs, A.; Horst, R.; Wolf, B. A. *J. Macromol. Sci., Part A: Pure Appl. Chem.* **1996**, *33*, 1097–1111.
- (70) Gelles, R.; Frank, C. W. *Macromolecules* **1983**, *16*, 1448–1456.
- (71) Yuan, Y.; Reece, T. J.; Sharma, P.; Poddar, S.; Ducharme, S.; Gruverman, A.; Yang, Y.; Huang, J. *Nat. Mater.* **2011**, *10*, 296–302.
- (72) Schilinsky, P.; Asawapirom, U.; Scherf, U.; Biele, M.; Brabec, C. J. *Chem. Mater.* **2005**, *17*, 2175–2180.
- (73) Ballantyne, A. M.; Chen, L.; Dane, J.; Hammant, T.; Braun, F. M.; Heaney, M.; Duffy, W.; McCulloch, I.; Bradley, D. D. C.; Nelson, J. *Adv. Funct. Mater.* **2008**, *18*, 2373–2380.